Magnetochemistry **2015**, *1*, 3-16 doi:10.3390/magnetochemistry1010003

OPEN ACCESS

magnetochemistry

ISSN 2312-7481

www.mdpi.com/journal/magnetochemistry

Article

Synthesis of 4-Hydroxy-2,6-di(pyrazol-1-yl)pyridine, and the Spin State Behaviour of Its Iron(II) Complex Salts

Laurence J. Kershaw Cook and Malcolm A. Halcrow *

School of Chemistry, University of Leeds, Woodhouse Lane, Leeds LS2 9JT, UK;
E-Mail: ljkcook@gmail.com

* Author to whom correspondence should be addressed; E-Mail: m.a.halcrow@leeds.ac.uk;
Tel.: +44-113-343-6506; Fax: +44-113-343-6565.

Academic Editor: Guillem Aromí

Received: 3 September 2015 / Accepted: 12 October 2015 / Published: 23 October 2015

Abstract: Treatment of 4-hydroxy-2,6-dibromopyridine with four equivalent of deprotonated pyrazole in hot diglyme affords 4-hydroxy-2,6-di(pyrazol-1-yl)pyridine (*L*) in low yield. The three complex salts [Fe*L*$_2$]X_2 (X^- = BF_4^-, **1**; X^- = ClO_4^-, **2**; X^- = PF_6^-, **3**) have been prepared, and crystallographically characterised as their methanol solvates. The solvate structures contain complexes that are fully high-spin (**1** and **3**), or in a mixed high:low spin state population at 150 K (**2**). Bulk samples of **1** and **2** obtained from methanol/diethyl ether contain a second, minor crystal phase that exhibits an abrupt spin-transition near 200 K. Recrystallisation of **1** and **2** from nitromethane/diethyl ether affords powder samples that are highly enriched in this spin-transition phase.

Keywords: iron; *N*-donor ligand; spin-crossover; crystal structure; magnetic measurements; calorimetry

1. Introduction

The $[Fe(bpp)_2]^{2+}$ (bpp = 2,6-di{pyrazol-1-yl}pyridine) family of complexes [1–3] is widely used in the field of spin-crossover research (Scheme 1) [4,5]. While they often undergo spin-crossover near room-temperature [1], the particular advantage of this class of compounds is that synthetic methods are available to functionalise every position of the bpp ligand framework [6]. Pyridyl *C*4 substituents ("R" in Scheme 1) are of particular use, since they allow functionality to be introduced onto the complex without exerting a steric influence on the metal coordination sphere. This has allowed multifunctional

compounds combining spin-crossover with fluorescence [7], redox activity [8], photo-isomerisable substituents [9] and tether groups [10–12] to be produced based on $[Fe(bpp)_2]^{2+}$ switching centres.

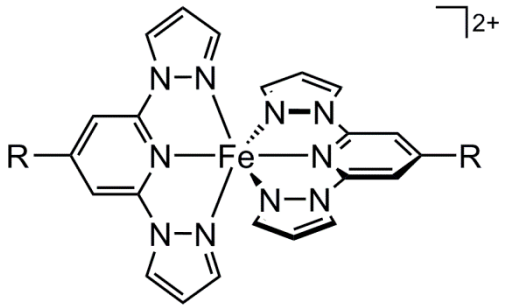

Scheme 1. The structure of the $[Fe(bpp)_2]^{2+}$ family of complexes ($[Fe(bpp)_2]^{2+}$ itself has R = H, $[FeL_2]^{2+}$ has R = OH).

Continuing our own interest in $[Fe(bpp)_2]^{2+}$ derivatives [1,3], we have pursued ways to introduce new functional groups onto the bpp ligand. After describing the first bpp derivatives bearing sulfur-based "*R*" substituents [13–15], we have turned to bpp ligands with oxygen-based "*R*" groups which were also unknown up to now. We were inspired by Real *et al.*'s reports of salts of $[Co(terpyOH)_2]^{2+}$ (terpyOH = 4′-hydroxy-2,2′:6′,2″-terpyridine) [16–18], which exhibit noteworthy spin-crossover cooperativity including a rare "reverse" spin-transition [18]. We report here the corresponding ligand from the bpp series, 4-hydroxy-2,6-di(pyrazol-1-yl)pyridine (*L*), and its iron complex salts. Since complexes related to $[Co(bpp)_2]^{2+}$ are high-spin [19], $[CoL_2]^{2+}$ was not investigated in this study because the *L* ligand was only available in small quantities.

2. Results and Discussion

2.1. Synthesis

Following the usual protocol for the synthesis of bpp derivatives [20], treatment of 2,6-dibromo-4-hydroxypyridine [21] with 4 equiv. K[pz] in hot diglyme for 3 days afforded *L* in 11% yield after purification by silica column chromatography (Scheme 2). While the yield of *L* is low, it was sufficient to explore its coordination chemistry. Despite the excess of pyrazole used, a significant quantity of the monosubstituted by-product 2-bromo-4-hydroxy-6-(pyrazol-1-yl)pyridine (*L*′, Scheme 2) was also isolated from the reaction, implying that the second substitution step in the reaction is sluggish [22,23]. An attempt to obtain improved yields of *L* by THP-protection of the 2,6-dibromo-4-hydroxy-pyridine hydroxyl function (THP = tetrahydropyran-2-yl [24]) was unsuccessful, since displacement of the protected O–THP group occurred during the pyrazole coupling step. Although we did not obtain its crystal structure, NMR data in $(CD_3)_2SO$ demonstrate that *L* adopts the hydroxypyridine tautomer shown in Scheme 2, rather than the alternative pyridone form preferred by terpyOH in condensed phases [25]. Evidence includes the O*H* proton resonance at 11.5 ppm (the N*H* proton peak from a pyridone tautomer would come near 7 ppm); and, the pyridyl *C*4 chemical shift of 168.4 ppm (the pyridone tautomer would have a C=O group at this position, resonating near 180 ppm) [25].

The salts [FeL_2]X_2 (X^- = BF_4^-, **1**; X^- = ClO_4^-, **2**; X^- = PF_6^-, **3**) were obtained by complexing 0.5 equiv. of the appropriate iron(II) salt by *L* in nitromethane, which yielded the products as yellow microcrystals after the usual work-up.

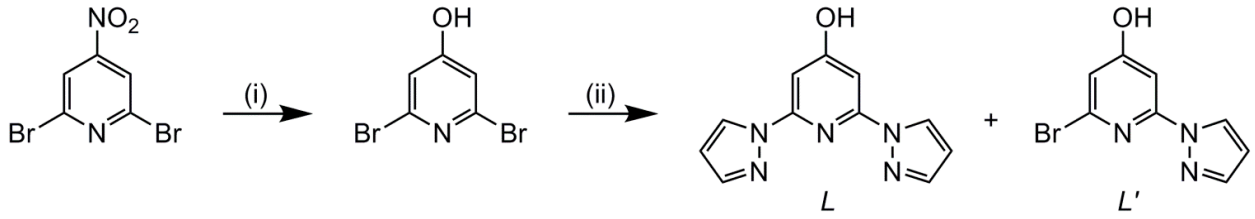

Scheme 2. Synthesis of *L*. Reagents and conditions: (i) NBu_4OH (aq), thf, 48 h, 298 K; 70% [20]; (ii) K[pz] (4 equiv), diglyme, 180 °C, 3 days then HCl (aq); 11% (*L*) and 24% (*L′*).

2.2. Crystallographic Characterisation

Methanol solvate crystals of **1**–**3** were obtained by slow crystallisation from MeOH/Et_2O, and characterised at low temperature (100 or 150 K). Crystals of **2**·1.75MeOH·0.25H_2O and **3**·2MeOH are isostructural (orthorhombic, *Pccn*, *Z* = 8) and, while **1**·2MeOH (monoclinic, *C*2/*c*, *Z* = 4) is not isostructural with the other two salts it shows several similarities with them. All the crystals contain the expected six-coordinate $[FeL_2]^{2+}$ cation, which is C_2-symmetric in **1**·2MeOH but has no crystallographically-imposed symmetry in the other two salts (Figures 1 and 2).

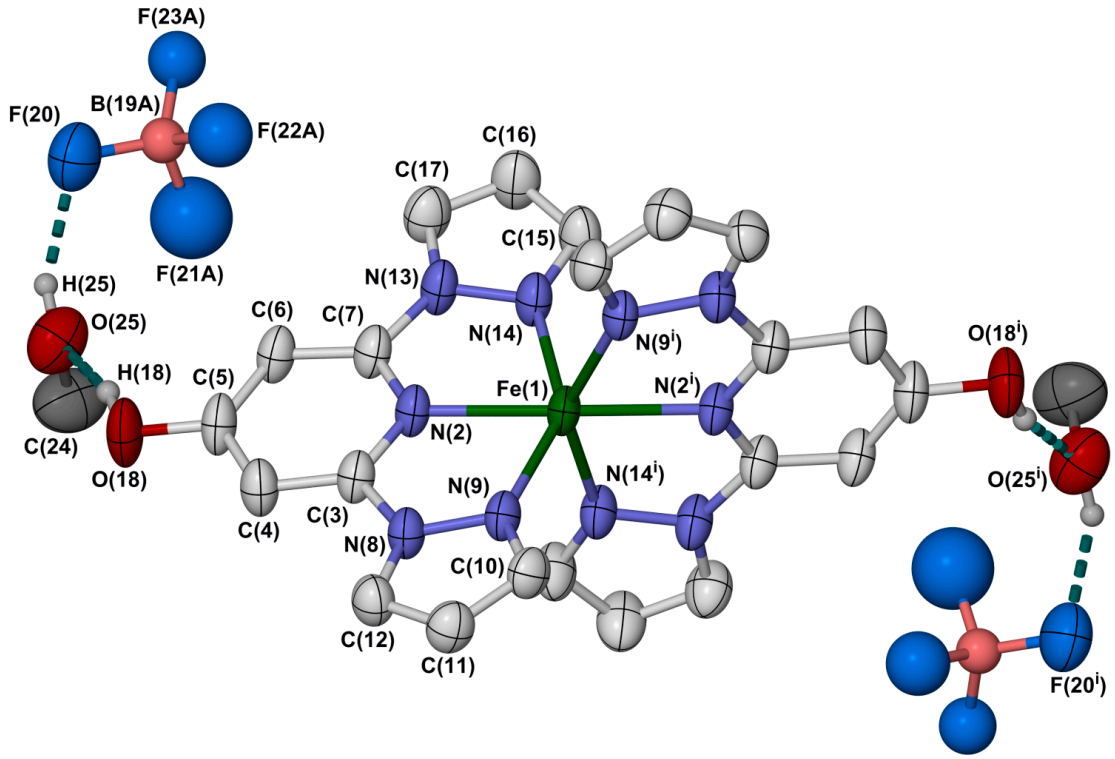

Figure 1. View of the hydrogen bonded formula unit in **1**·2MeOH. Atomic displacement ellipsoids are at the 50% probability level. Only one orientation of the disordered BF_4^- ion is shown, and *C*-bound H atoms have been omitted. Colour code: C, white; H, pale grey; B, pink; F, cyan; Fe, green; O, red. Symmetry code: (i) −*x*, *y*, 1/2−*z*.

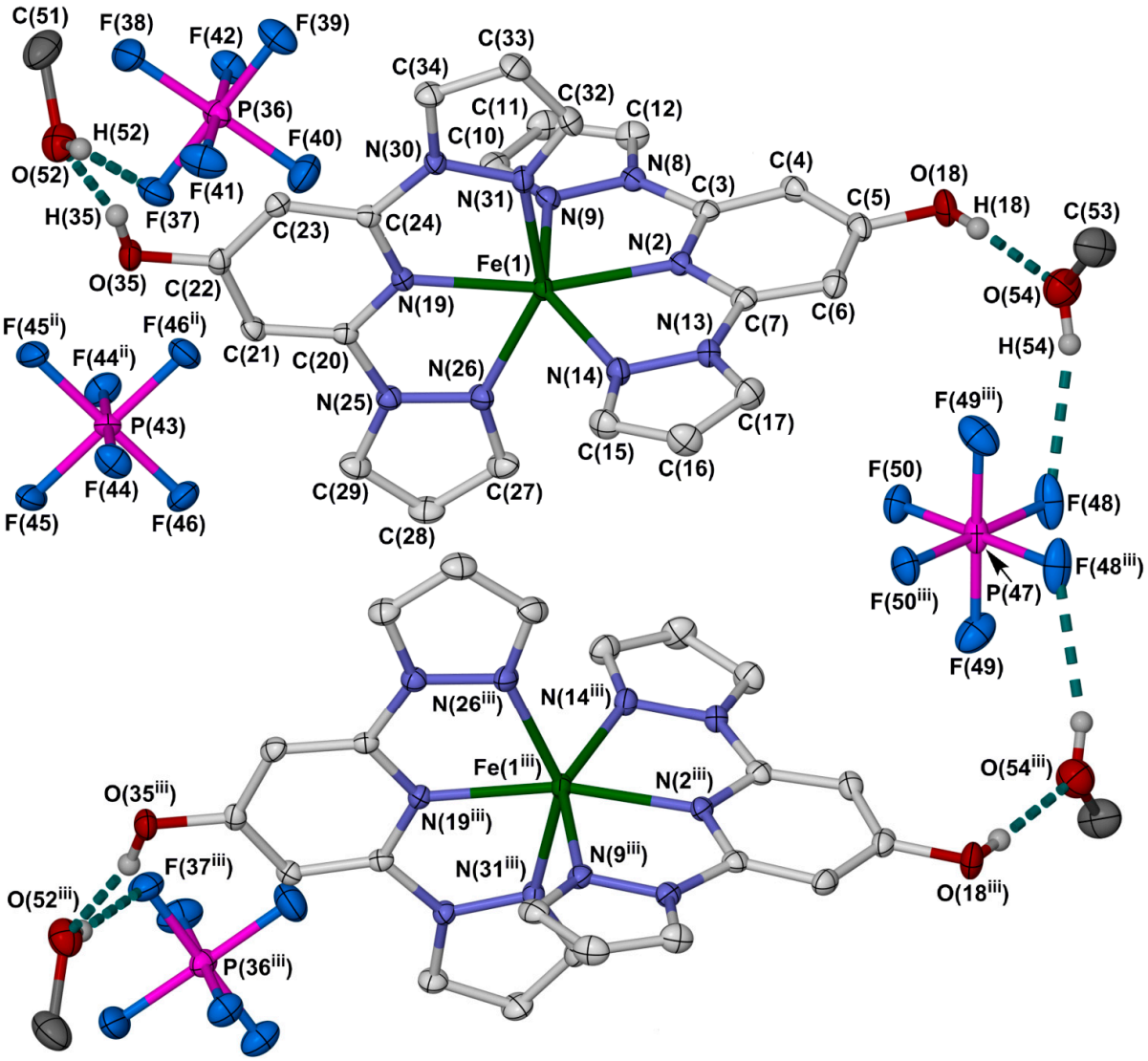

Figure 2. View of the hydrogen bonded assembly of two asymmetric units of **3**·2MeOH. Crystals of **2**·1.75MeOH·0.25H_2O are isostructural to this one, but exhibit additional anion and solvent disorder. Colour code: C, white; H, pale grey; F, cyan; Fe, green; O, red; P, purple. Other details as for Figure 1. Symmetry codes: (ii) 1/2−*x*, 1/2−*y*, *z*; (iii) 3/2−*x*, 1/2−*y*, *z*.

The metric parameters in the structures show that the iron centres in **1**·2MeOH and **3**·2MeOH are fully high-spin at the temperature of measurement (Table 1). That is most evident in the parameters Σ and Θ, which are calculated from the N–Fe–N bond angles in the complex and are particularly sensitive to the spin state population of the iron centre [26,27]. In contrast Σ, Θ and the Fe–N distances in **2**·1.75MeOH·0.25H_2O are somewhat lower than in the other two structures, which implies that $[FeL_2]^{2+}$ contains a mixture of high-spin and low-spin molecules at 150 K. However, in view of the magnetic data described below, it is unclear whether the spin-state population of **2**·1.75MeOH·0.25H_2O at 150 K is temperature-independent, or indicative of thermal spin-crossover.

Table 1. Selected bond distances (Å) and angular parameters (°) for the crystal structures in this work. α, Σ and Θ are indices characteristic for the spin state of the complex [26,27], while θ and ϕ are measures of the Jahn-Teller distortion sometimes shown by these iron centers in their high-spin state [28]. Typical values of these parameters in $[Fe(bpp)_2]^{2+}$ derivatives are given in ref. [1].

Compound	**1·2MeOH**	**2·1.75MeOH·0.25H$_2$O**	**3·2MeOH**
T (K)	150	150	100
Fe(1)−N(2)	2.147(3)	2.0665(19)	2.1204(16)
Fe(1)−N(9)	2.217(3)	2.138(3)	2.1936(17)
Fe(1)−N(14)	2.208(3)	2.137(2)	2.1860(17)
Fe(1)−N(19)	-	2.069(2)	2.1237(16)
Fe(1)−N(26)	-	2.116(3)	2.1630(17)
Fe(1)−N(31)	-	2.135(2)	2.1852(17)
α	73.22(15)	75.51(16)	73.35(12)
Σ	153.7(4)	130.7(3)	153.0(2)
Θ	481	414	477
ϕ	165.55(15)	169.06(7)	166.68(6)
θ	85.17(3)	86.67(3)	87.36(1)

The cations in all three structures deviate significantly from the idealised D_{2d} symmetry expected for a six-coordinate complex with this ligand combination. This structural distortion is often observed in high-spin $[Fe(bpp)_2]^{2+}$ derivatives [3], and is caused by a Jahn-Teller distortion of the orbitally degenerate high-spin iron(II) configuration [28]. The distorted structures can be quantified by two more parameters, ϕ and θ, that describe the relative dispositions of the *L* ligands in the molecule [1,28]. The most noteworthy aspect of **1**·2MeOH–**3**·2MeOH is their reduced values of ϕ, the *trans*-N{pyridyl}–Fe–N{pyridyl} angle, which range between $165.55(15) \leq \phi \leq 169.06(7)°$ in the three structures. For comparison, a complex with ideal D_{2d} symmetry would show $\phi = 180°$ [28]. We have previously proposed that complexes with $\phi < 172°$ should remain high-spin at all temperatures [1], which is consistent with the high-spin nature of **1**·2MeOH and **3**·2MeOH. However the activity of **2**·1.75MeOH·0.25H$_2$O towards spin-crossover is unexpected in that regard; although this structure has a slightly higher value of ϕ than **1** and **3** (Table 1), it is still lower than our proposed threshold value.

In each structure, the hydroxyl groups in the complex form O–H…O hydrogen bonds to methanol solvent molecules, which in turn donate a O–H…*X* (*X* = F or O) hydrogen bond to a neighbouring anion. In **1**·2MeOH, this leads to discrete $\{[FeL_2][MeOH]_2[BF_4]_2\}$ hydrogen bond assemblies in the lattice (Figure 1). In contrast, in **2**·1.75MeOH·0.25H$_2$O and **3**·2MeOH one anion lying on a crystallographic inversion centre accepts hydrogen bonds from two different methanol molecules, leading to $\{([FeL_2][MeOH]_2X)_2(\mu\text{-}X)\}^+$ (X^- = ClO_4^- or PF_6^-) assembly structures (Figure 2). In each case, the hydrogen-bond assemblies in the lattice only interact with their neighbours through weak van der Waals contacts. The hydrogen bonded anions and solvent in **2**·1.75MeOH·0.25H$_2$O suffer from disorder, but are crystallographically ordered in isostructural **3**·2MeOH. That may also influence the different spin-state properties of those crystals.

2.3. Characterisation of the Bulk Materials

The lattice solvent is lost from all the methanol solvates upon exposure to air, yielding solvent-free powders by microanalysis (referred to as **1**^{m}–**3**^{m}). While **3**^{m} is high-spin at all temperatures, magnetic susceptibility data imply that bulk samples of **1**^{m} and **2**^{m} are not phase-pure. In both samples, 15%–25% of the solid exhibits an abrupt spin-transition at 210–220 K, with the remaining material being fully high-spin (**1**^{m}) or low-spin (**2**^{m}; Figure 3). The approximate 1:3 high-spin:low-spin population in **2**^{m} at room temperature, predicted by the magnetic data, is consistent with its colouration which is noticably darker than for **1**^{m} or **3**^{m}. However, the low-spin nature of **2**^{m} at 150 K from these data contrasts with the crystal structure of the parent solvate **2**·1.75MeOH·0.25H_2O which is *ca.* 65% high-spin at that temperature. We conclude that the spin-state behaviour of **3**^{m} and the main component of **1**^{m} is unaffected by desolvation of the parent methanol solvate materials. However, removal of the solvent from **2**·1.75MeOH·0.25H_2O, to form **2**^{m}, has a strong effect on the properties of the complex. Changes of spin state induced by removal of lattice solvent are well known in the literature [8,29,30].

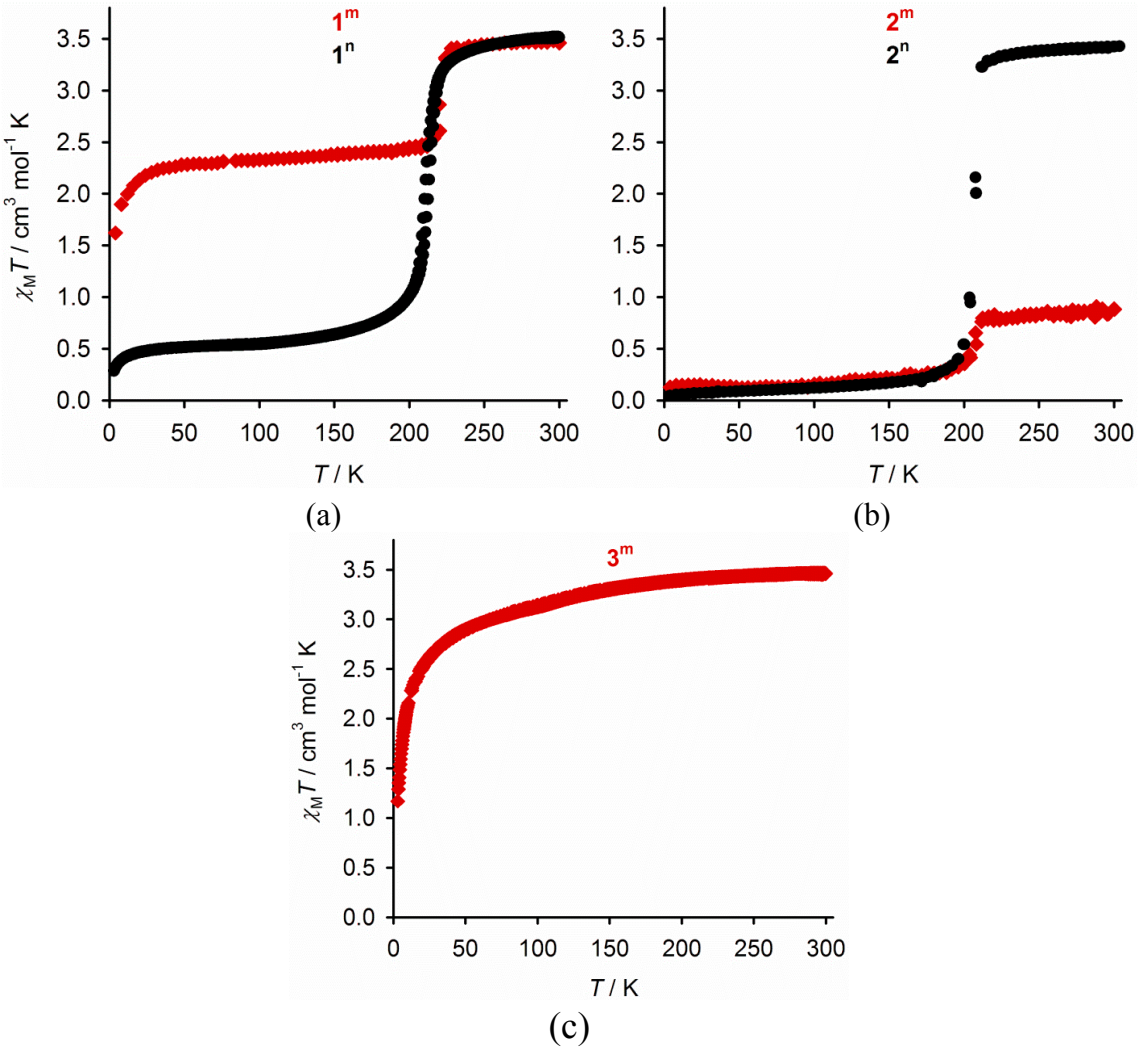

Figure 3. Variable temperature magnetic susceptibility data for **1** (**a**), **2** (**b**) and **3** (**c**). The black circles are from samples crystallised from nitromethane/diethyl ether (**1**^{n} and **2**^{n}), and the red diamonds are material obtained from methanol/diethyl ether (**1**^{m}, **2**^{m} and **3**^{m}).

The partial, abrupt spin-transitions shown by bulk samples of $\mathbf{1}^{\mathbf{m}}$ and $\mathbf{2}^{\mathbf{m}}$ are probably associated with a second crystal phase of the complexes. Consistent with that suggestion, recrystallisation of **1** and **2** from nitromethane/diethyl ether afforded new solvent-free powders $\mathbf{1}^{\mathbf{n}}$ and $\mathbf{2}^{\mathbf{n}}$, which now have the same pale yellow colouration. These exhibit abrupt spin-transitions at the same temperatures as the minor phases in the methanolic samples (Figure 3). The transition in $\mathbf{1}^{\mathbf{n}}$ exhibits $T_{½}$ = 211 K and is 78% complete at 150 K, suggesting there is still a minor fraction of a high-spin phase in this new sample.

In contrast, the transition in $\mathbf{2}^{\mathbf{n}}$ is centred at $T_{½}$ = 207 K and proceeds to completeness, implying that sample is phase-pure. Both spin transitions exhibit a narrow 1–2 K thermal hysteresis in the SQUID magnetometer at a scan rate of 2 $Kmin^{-1}$, which we have also observed in a number of other compounds from the $[Fe(bpp)_2]^{2+}$ family [31,32].

These observations were confirmed by DSC measurements (Figure 4), which afforded thermodynamic parameters for the transitions that are similar to those shown by the parent compound $[Fe(bpp)_2][BF_4]_2$ [28]. For $\mathbf{1}^{\mathbf{n}}$: $T_{½}\downarrow$ = 209 K, $T_{½}\uparrow$ = 215 K, ΔH = 22.4 $kJmol^{-1}$ and ΔS = 106 $Jmol^{-1}K^{-1}$ (corrected for the incompleteness of the transition). For $\mathbf{2}^{\mathbf{n}}$: $T_{½}\downarrow$ = 205 K, $T_{½}\uparrow$ = 210 K, ΔH = 21.7 $kJmol^{-1}$ and ΔS = 105 $Jmol^{-1}K^{-1}$. The wider thermal hysteresis in these data, compared to the magnetic susceptibility measurements, is probably a consequence of the more rapid thermal scan rate of 10 $Kmin^{-1}$ that was used in the DSC experiments [33]. The errors on the measured thermodynamic parameters will also be relatively large, because the transitions lie near the lower temperature limit for our calorimeter (Figure 4).

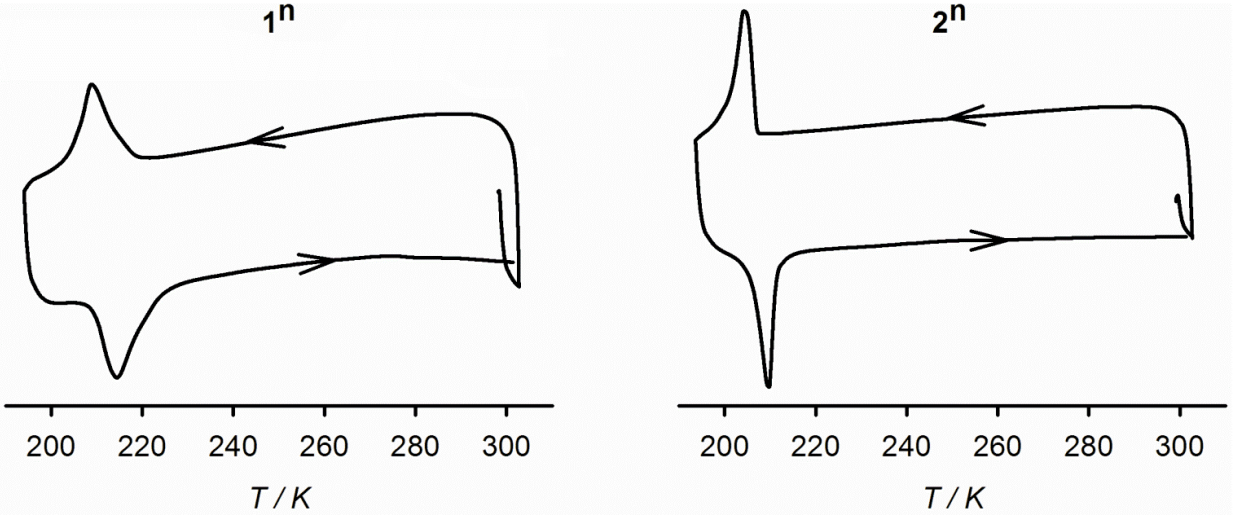

(a) (b)

Figure 4. DSC data for $\mathbf{1}^{\mathbf{n}}$ (**a**) and $\mathbf{2}^{\mathbf{n}}$ (**b**).

X-ray powder diffraction data at 298 K showed that the spin-transition phases of $\mathbf{1}^{\mathbf{n}}$ and $\mathbf{2}^{\mathbf{n}}$ are isostructural, and unrelated to the methanol solvate structures (Figure 5). Since there is no apparent crystalline contaminant in the powder pattern of $\mathbf{1}^{\mathbf{n}}$, the residual high-spin fraction of this sample may arise from amorphous material. The isolation of the spin-transition phases from two different solvent mixtures implies they should be solvent-free forms of the complexes. However, that remains to be confirmed since we have been unable to obtain these phases as single crystals.

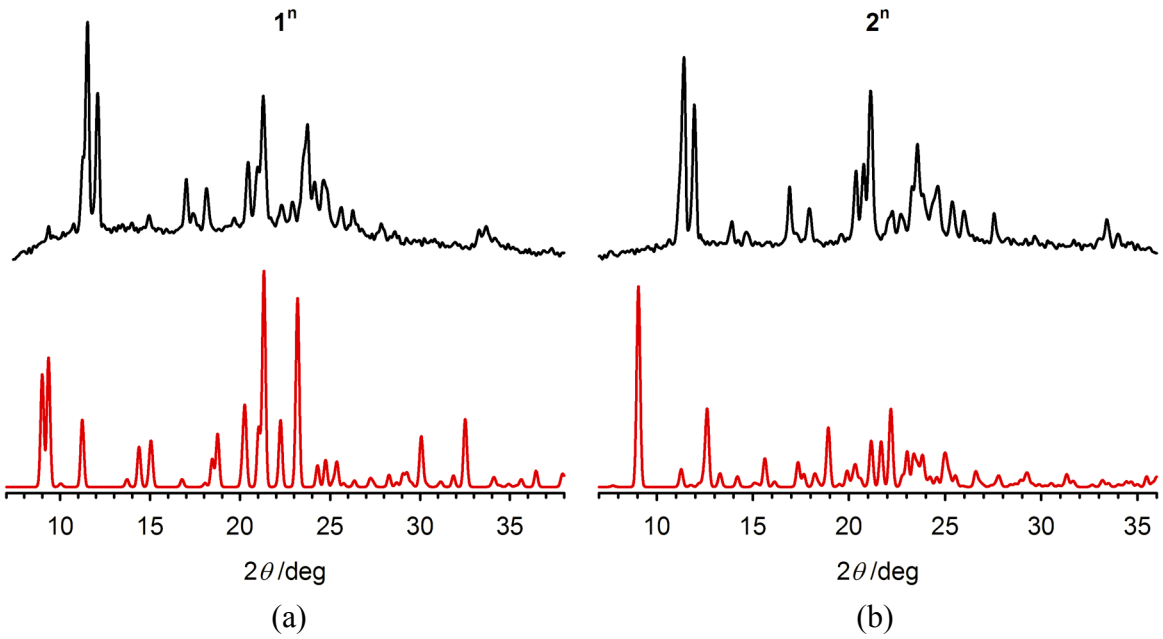

Figure 5. Experimental X-ray powder diffraction patterns (black) of the spin-crossover active phases **1**^{n} (**a**) and **2**^{n} (**b**), and simulations based on their methanol solvate crystal structures (red). The black traces are isostructural with each other, but not with the red traces.

3. Experimental Section

3.1. Instrumentation

Elemental microanalyses were performed by the University of Leeds School of Chemistry microanalytical service. ^{1}H-NMR spectra employed a Bruker (Coventry, UK) DPX300 spectrometer operating at 300.2 MHz (^{1}H) or 75.5 MHz (^{13}C). Electrospray mass spectra (ESI MS) were obtained on a Waters (Elstree, UK) ZQ4000 spectrometer, from MeCN feed solutions. All mass peaks have the correct isotopic distributions for the proposed assignments. X-ray powder diffraction patterns were measured using a Bruker (Coventry, UK) D2 Phaser diffractometer. DSC measurements used a TA (Elstree, UK) Instruments DSC Q20 calorimeter, heating at a rate of 10 Kmin^{-1}. Solid state magnetic susceptibility measurements were performed on a Quantum Design (Leatherhead, UK) SQUID or SQUID/VSM magnetometer, in an applied field of 1000 or 5000 G with a scan rate of 2 K·min^{-1}. A diamagnetic correction for the sample was estimated from Pascal's constants [34], and a previously measured diamagnetic correction for the sample holder was applied.

3.2. Synthesis

3.2.1. Synthesis of 4-Hydroxy-2,6-di(pyrazol-1-yl)pyridine (*L*) and 2-Bromo-4-Hydroxy-6-(pyrazol-1-yl)pyridine (*L′*)

Pyrazole (3.1 g, 45.5 mmol) was added to a stirred suspension of KH (1.6 g, 39.6 mmol) in dry diglyme (45 cm^{3}) at 70 °C. When H_2 evolution had ceased, 4-hydroxy-2,6-dibromopyridine (2.6 g, 10.3 mmol) [21] was added and the mixture was then heated at 180 °C for 3 days. After cooling to room temperature, the diglyme was removed *in vacuo* and the brown residue carefully dissolved in H_2O. The

solution was filtered, then neutralised with HCl affording a pale brown precipitate which was collected on a glass sinter. Silica gel column chromatography of the crude material (eluent 1:1 dichloromethane:ethyl acetate) yielded the two products as colourless solids.

For *L* (R_f 0.29). Yield 0.26 g, 11%. Found: C, 56.4; H, 3.90; N, 29.4%. Calcd for $C_{11}H_9N_5O{\cdot}½H_2O$ C, 55.9; H, 4.26; N, 29.6%. M.p. 214–216 °C. ES mass spectrum: *m*/*z* 250.1 ([Na*L*]$^+$). ^{1}H-NMR spectrum ({CD_3}$_2$SO): δ 6.58 (dd, 1.9 and 2.0 Hz, 2H, Pz *H*^{4}), 7.21 (s, 2H, Py *H*$^{3/5}$), 7.82 (d, 1.9 Hz, 2H, Pz *H*^{3}), 8.86 (d, 2.0 Hz, 2H, Pz *H*^{5}), 11.50 (br s, 1H, O*H*). ^{13}C-NMR spectrum ({CD_3}$_2$SO): δ 96.4 (2C, Py *C*$^{3/5}$), 108.0 (2C, Pz *C*^{4}), 128.0 (2C, Pz *C*^{5}), 142.3 (2C, Pz *C*^{3}), 151.0 (2C, Py *C*$^{2/6}$), 168.4 (1C, Py *C*^{4}).

For *L*′ (R_f 0.78). Yield 0.57 g, 24%. M.p. 218–220 °C. Found: C, 43.7; H, 3.90; N, 13.9%. Calcd for $C_8H_6BrN_3O{\cdot}½C_2H_5O_2CCH_3$ C, 44.2; H, 4.22; N, 14.1%. ES mass spectrum: *m*/*z* 262.0 [Na*L*′]$^+$. ^{1}H-NMR spectrum ({CD_3}$_2$SO): δ 6.56 (dd, 2.1 and 2.2 Hz, 1H, Pz *H*^{4}), 6.92 (d, 1.7 Hz, 1H, Py *H*^{3}), 7.29 (d, 1.7 Hz, 1H, Py *H*^{5}), 7.81 (d, 2.1 Hz, 1H, Pz *H*^{3}), 8.46 (d, 2.2 Hz, 1H, Pz *H*^{5}) 11.65 (br s, 1H, O*H*). ^{13}C-NMR spectrum ({CD_3}$_2$SO): δ 98.3 (1C, Py *C*^{5}), 108.4 (1C, Pz *C*^{4}), 113.1 (1C, Py *C*^{3}), 127.4 (1C, Pz *C*^{5}), 140.1 (1C, Pz *C*^{3}), 142.6 (1C, Py *C*^{2}), 151.9 (1C, Py *C*^{6}), 167.7 (1C, Py *C*^{4}).

3.2.2. Synthesis of the Complexes

The same basic method, described below for [Fe*L*$_2$][BF_4]$_2$, was used for all the complexes in this work. A solution of *L* (0.20 g, 0.88 mmol) and Fe[BF_4]$_2{\cdot}6H_2O$ (0.15 g, 0.44 mmol) in nitromethane (15 cm^3) was refluxed until all the solid had dissolved (*ca.* 2 h). The cooled solution was concentrated *in vacuo* to *ca.* 5 cm^3. Slow diffusion of diethyl ether vapour into the filtered solution afforded yellow microcrystals of the product. The other complex salts were prepared using analogous reactions, with appropriate amounts of Fe[ClO_4]$_2{\cdot}6H_2O$ or Fe[PF_6]$_2$, as required (Fe[PF_6]$_2$ was prepared *in situ* by treating $FeCl_2{\cdot}4H_2O$ with 2 equiv. $AgPF_6$. The precipitated AgCl was removed by filtration before addition of the *L* ligand). Yields ranged from 34%–75%.

For [Fe*L*$_2$][BF_4]$_2$ (**1**): found C, 38.6; H, 2.60; N, 20.5%. Calcd for $C_{22}H_{18}B_2F_8FeN_{10}O_2$ C, 38.6; H, 2.65; N, 20.5%.

For [Fe*L*$_2$][ClO_4]$_2$ (**2**): found C, 36.9; H, 2.40; N, 19.6%. Calcd for $C_{22}H_{18}Cl_2FeN_{10}O_{10}$ C, 37.3; H, 2.56; N, 19.8%.

For [Fe*L*$_2$][PF_6]$_2$ (**3**): found C, 32.9; H, 2.30; N, 17.2%. Calcd for $C_{22}H_{18}F_{12}FeN_{10}O_2P_2$ C, 33.0; H, 2.27; N, 17.5%.

3.3. Crystal Structure Determinations

The single crystals were grown by slow diffusion of diethyl ether vapour into methanol solutions of the complexes. Diffraction data for **1**·2MeOH and **2**·1.75MeOH·0.25H_2O were measured using a Bruker (Coventry, UK) X8 Apex diffractometer, with graphite-monochromated Mo-K_α radiation (λ = 0.71073 Å) generated by a rotating anode. Data for **3**·2MeOH were collected with an Agilent (Stockport, UK) Supernova dual-source diffractometer using monochromated Cu-K_α radiation (λ = 1.54184 Å). Experimental details of the structures determinations in this study are given in Table 2. All the structures were solved by direct methods *(SHELXS97* [35]), and developed by full least-squares refinement on F^2 (*SHELXL97* [35]). Crystallographic figures were prepared using *XSEED* [36].

Table 2. Experimental details for the crystal structures in this work.

Compound	**1·2MeOH**	**2·1.75MeOH·0.25H$_2$O**	**3·2MeOH**
formula	$C_{24}H_{26}B_2F_8FeN_{10}O_4$	$C_{23.75}H_{25.5}Cl_2FeN_{10}O_{12}$	$C_{24}H_{26}F_{12}FeN_{10}O_2P_2$
M_r	748.02	769.79	864.34
crystal class	monoclinic	orthorhombic	orthorhombic
space group	*C*2/*c*	*Pccn*	*Pccn*
a/Å	23.635(3)	12.478(3)	12.4620(2)
b/Å	11.8299(12)	28.434(6)	28.4031(4)
c/Å	15.7821(19)	18.806(4)	18.7480(3)
β/°	131.720(7)	-	-
V/Å^3	3293.6(7)	6672(3)	6636.03(18)
Z	4	8	8
T/K	150(2)	150(2)	100(2)
D_{calcd}/Mg·m^{-3}	1.508	1.533	1.730
μ/mm^{-1}	0.551 [a]	0.686 [a]	5.649 [b]
measured reflections	30968	214641	17673
unique reflections	3980	11663	6582
observed reflections	3382	8429	5707
R_{int}	0.066	320.080	0.025
R_1 [$F_o > 4\sigma(F_o)$] [c]	0.076	0.059	0.033
wR_2 [all data] [d]	0.230	0.168	0.083
GoF	1.065	1.051	1.040
Δρmax, Δρmin/*e*Å^{-3}	1.43, −0.65	0.75, −0.56	1.40, −0.47

[a] Collected with Mo-K_α radiation; [b] Collected with Cu-K_α radiation; [c] $R = \Sigma[|F_o| - |F_c|]/\Sigma|F_o|$; [d] $wR = [\Sigma w(F_o^2 - F_c^2)/\Sigma wF_o^4]^{1/2}$.

CCDC-1006318 (**1**·2MeOH), CCDC-1006319 (**2**·1.75MeOH·0.25H$_2$O) and CCDC-1006320 (**3**·2MeOH) contain the supplementary crystallographic data for this paper. These data can be obtained free of charge from The Cambridge Crystallographic Data Centre via www.ccdc.cam.ac.uk/data_request/cif.

3.3.1. Structure Refinement of **1**·2MeOH

This structure was solved in $P\bar{1}$, then transformed up to *C*2/*c* using the *ADSYMM* routine in *PLATON* [37]. The asymmetric unit contains half a formula unit, with Fe(1) lying on the crystallographic C_2 axis 0, *y*, 1/4. The unique BF_4^- ion is disordered, and was refined over three sites with occupancies of 0.5:0.3:0.2. These three partial anions share a common wholly occupied F atom, and were modelled using the refined restraints B–F = 1.39(2) and F...F = 2.27(2) Å. All non-H atoms with occupancy ≥0.5 were refined anisotropically, while H atoms were placed in calculated positions and refined using a riding model. The highest residual Fourier peak of +1.4 *e*Å^{-3} is 0.9 Å from Fe(1).

3.3.2. Structure Refinement of **2**·1.75MeOH·0.25H$_2$O

This structure was originally solved in $P2_1/c$, then transformed to *Pccn* using *PLATON* as before [37]. The asymmetric unit contains one complex dication, one crystallographically ordered anion; two disordered half-anions lying on special positions; and two solvent sites. Both disordered half-anions were modelled

over two orientations with a 0.3:0.2 occupancy ratio. The refined restraints Cl–O = 1.46(2) and O...O = 2.38(2) Å were applied to these partial anion sites. One of the solvent sites contains a crystallographically ordered methanol molecule, but the other was refined as a mixture of methanol (refined occupancy 0.75) and water (0.25). These residues were modelled without restraints. All non-H atoms with occupancy >0.5, plus all the partial Cl atoms, were refined anisotropically. All H atoms in the complex dications and methanol molecules were placed in calculated positions and refined using a riding model. H atoms from the partial water molecule were not located, and could not be included in the final model. They are accounted for in the density and *F*(000) calculations, however.

3.3.3. Structure Refinement of **3**·2MeOH

The solvated PF_6^- salt is isostructural with **2**·1.75MeOH·0.25H_2O, but does not suffer from the same anion or solvent disorder at the temperature of measurement (100 K). No disorder was detected during refinement of this structure and no restraints were applied to the model. A residual Fourier peak of +1.4 eÅ^{-3} occupies the same position as the fractional water content in the perchlorate structure, but this refined to <10% occupancy and so was not included in the final model.

4. Conclusions

The synthesis of 4-hydroxy-2,6-di(pyrazol-1-yl)pyridine (*L*) has been achieved, in two steps from commercially available precursors with a low but usable yield. Compound *L* is the first ligand from the bpp family with an oxygen substituent at the pyridine ring (Scheme 1). Three salts of $[Fe\mathit{L}_2]^{2+}$ have been prepared, and crystallographically characterised as their methanol solvates. While two of these remain high-spin at low-temperature, the solvated perchlorate salt (**2**) exhibits a mixed high/low spin state population at 150 K. Notably **2**·1.75MeOH·0.25H_2O also exhibits significant anion and solvent disorder at low temperature, whereas high-spin **3**·2MeOH does not. The different spin state properties of the two isostructural crystals may be related to this disorder, which would result in a less rigid lattice environment around the complex molecule in the perchlorate salt.

Bulk samples of **1** and **2** isolated from methanol/diethyl ether, $\mathbf{1^m}$ and $\mathbf{2^m}$, appear to contain a second, solvent-free contaminant phase that undergoes an abrupt spin-transition near 200 K. Samples enriched in the latter phase, $\mathbf{1^n}$ and $\mathbf{2^n}$, are obtained by recrystallising from nitromethane/diethyl ether which has allowed the spin-transition to be properly characterised. While a crystal structure of $\mathbf{1^n}$ and $\mathbf{2^n}$ was not achieved, the form of their spin transitions is reminiscent of other complexes from the $[Fe(bpp)_2]^{2+}$ family, that adopt a particular type of crystal packing (the "terpyridine embrace") [31].

Our future work is aimed towards using *L* as a precursor to $[Fe(bpp)_2]^{2+}$ derivatives bearing other oxygen-based functionalities (Scheme 1; R = OR', O_2CR' *etc*. where R' = alkyl or aryl).

Acknowledgments

The authors thank Oscar Cespedes (University of Leeds) and Floriana Tuna (University of Manchester) for help with the magnetic measurements. This work was funded by the EPSRC (EP/H015639/1 and EP/K00512X/1).

Author Contributions

L.J.K.C. performed the experimental work, while M.A.H. initiated and guided the study. Both authors contributed to the preparation of the manuscript.

Conflicts of Interest

The authors declare no conflict of interest.

References and Notes

1. Halcrow, M.A. Iron(II) complexes of 2,6-di(pyrazol-1-yl)pyridines—A versatile system for spin-crossover research. *Coord. Chem. Rev.* **2009**, *253*, 2493–2514.
2. Olguín, J.; Brooker, S. Spin crossover active iron(II) complexes of selected pyrazole-pyridine/pyrazine ligands. *Coord. Chem. Rev.* **2011**, *255*, 203–240.
3. Kershaw Cook, L.J.; Mohammed, R.; Sherborne, G.; Roberts, T.D.; Alvarez, S.; Halcrow, M.A. Spin state behaviour of iron(II)/dipyrazolylpyridine complexes. new insights from crystallographic and solution measurements. *Coord. Chem. Rev.* **2015**, *289–290*, 2–12.
4. Gütlich, P.; Goodwin, H.A. (Eds.) *Spin Crossover in Transition Metal Compounds I-III. Topics in Current Chemistry Vols. 233–235*; Springer: Berlin, Germany, 2004.
5. Halcrow M.A. (Ed.) *Spin-Crossover Materials—Properties and Applications*; John Wiley & Sons: Chichester, UK, 2013; p. 568.
6. Halcrow, M.A. Recent advances in the synthesis and applications of 2,6-dipyrazolylpyridine derivatives and their complexes. *New J. Chem.* **2014**, *38*, 1868–1882.
7. González-Prieto, R.; Fleury, B.; Schramm, F.; Zoppellaro, G.; Chandrasekar, R.; Fuhr, O.; Lebedkin, S.; Kappes, M.; Ruben, M. Tuning the spin-transition properties of pyrene-decorated 2,6-bispyrazolylpyridine based Fe(II) complexes. *Dalton Trans.* **2011**, *40*, 7564–7570.
8. Nihei, M.; Han, L.; Oshio, H. Magnetic bistability and single-crystal-to-single-crystal transformation induced by guest desorption. *J. Am. Chem. Soc.* **2007**, *129*, 5312–5313.
9. Hasegawa, Y.; Sakamoto, R.; Takahashi, K.; Nishihara, H. Solid-state ligand-driven light-induced spin change at ambient temperatures in bis(dipyrazolylstyrylpyridine)iron(II) complexes. *Inorg. Chem.* **2013**, *52*, 1658−1665.
10. Alam, M.S.; Stocker, M.; Gieb, K.; Müller, P.; Haryono, M.; Student, K.; Grohmann, A. Spin-state patterns in surface-grafted beads of iron(II) complexes. *Angew. Chem. Int. Ed.* **2010**, *49*, 1159–1163.
11. Devid, E.J.; Martinho, P.N.; Kamalakar, M.V.; Šalitroš, I.; Prendergast, U.; Dayen, J.-F.; Meded, V.; Lemma, T.; González-Prieto, R.; Evers, F.; *et al*. Spin transition in arrays of gold nanoparticles and spin crossover molecules. *ACS Nano* **2015**, *9*, 4496–4507.
12. Pukenas, L.; Benn, F.; Lovell, E.; Santoro, A.; Kershaw Cook, L.J.; Halcrow, M.A.; Evans, S.D. Bead-like structures and self-assembled monolayers from 2,6-dipyrazolylpyridines and their iron(II) complexes. *J. Mater. Chem. C* **2015**, *3*, 7890−7896.
13. Kershaw Cook, L.J.; Fisher, J.; Harding, L.P.; Halcrow, M.A. An iron(II) spin-crossover metallacycle from a back-to-back bis-[dipyrazolylpyridine]. *Dalton Trans.* **2015**, *44*, 9417–9425.

14. Kershaw Cook, L.J.; Shepherd, H.J.; Comyn, T.P.; Baldé, C.; Cespedes, O.; Chastanet, G.; Halcrow, M.A. Decoupled spin-crossover and structural phase transition in a molecular iron(II) complex. *Chem. Eur. J.* **2015**, *21*, 4805–4816.
15. Kershaw Cook, L.J.; Kulmaczewski, R.; Barrett, S.A.; Halcrow, M.A. Iron(II) complexes of 4-sulfanyl-, 4-sulfinyl- and 4-sulfonyl-2,6-dipyrazolylpyridine ligands. A subtle interplay between spin-crossover and crystallographic phase changes. *Inorg. Chem. Front.* **2015**, *2*, 662–670.
16. Gaspar, A.B.; Muñoz, M.C.; Niel, V.; Real, J.A. $[Co^{II}(4\text{-terpyridone})_2]X_2$: A novel cobalt(II) spin crossover system [4-terpyridone = 2,6-bis(2-pyridyl)-4(1*H*)-pyridone]. *Inorg. Chem.* **2001**, *40*, 9–10.
17. Galet, A.; Gaspar, A.B.; Muñoz, M.C.; Real, J.A. Influence of the counterion and the solvent molecules in the spin crossover system $[Co(4\text{-terpyridone})_2]X_{p}\cdot n H_2O$. *Inorg. Chem.* **2006**, *45*, 4413–4422.
18. Agustí, G.; Bartual, C.; Martínez, V.; Muñoz-Lara, F.J.; Gaspar, A.B.; Muñoz, M.C.; Real, J.A. Polymorphism and "reverse" spin transition in the spin crossover system $[Co(4\text{-terpyridone})_2](CF_3SO_3)_2\cdot 1H_2O$. *New J. Chem.* **2009**, *33*, 1262–1267.
19. Holland, J.M.; Kilner, C.A.; Thornton-Pett, M.; Halcrow, M.A. Steric effects on the electronic and molecular structures of nickel(II) and cobalt(II) 2,6-dipyrazol-1-ylpyridine complexes. *Polyhedron* **2001**, *20*, 2829–2840.
20. Jameson, D.L.; Goldsby, K.A. 2,6-Bis(*N*-pyrazolyl)pyridines: The convenient synthesis of a family of planar tridentate N_3 ligands that are terpyridine analogues. *J. Org. Chem.* **1990**, *55*, 4992−4994.
21. Vidonne, A.; Philp, D. Integrating replication processes with mechanically interlocked molecular architectures. *Tetrahedron* **2008**, *64*, 8464−8475.
22. Rodruígez-Ubis, J.C.; Sedano, R.; Barrosso, G.; Juanes, O.; Brunet, E. Lanthanide complexes of polyacid ligands derived from 2,6-bis(pyrazol-l-yl)pyridine, pyrazine, and 6,6′-bis(pyrazol-l-y1)-2,2′-bipyridine: Synthesis and luminescence properties. *Helv. Chim. Acta* **1997**, *80*, 86−96.
23. Yuan, J.; Wang, G.; Majima, K.; Matsumoto, K. Synthesis of a terbium fluorescent chelate and its application to time-resolved fluoroimmunoassay. *Anal. Chem.* **2001**, *73*, 1869−1876.
24. Elhaïk, J.; Pask, C.M.; Kilner, C.A.; Halcrow, M.A. Synthesis of 2,6-di(pyrazol-1-yl)-4-bromomethylpyridine, and its conversion to other 2,6-di(pyrazol-1-yl)pyridines substituted at the pyridine ring. *Tetrahedron* **2007**, *63*, 291–298.
25. Murguly, E.; Norsten, T.B.; Branda, N. Tautomerism of 4-hydroxyterpyridine in the solid, solution and gas phases: An X-ray, FT-IR and NMR study. *J. Chem. Soc. Perkin Trans.* **1999**, *2*, 2789–2794.
26. McCusker, J.K.; Rheingold, A.L.; Hendrickson, D.N. Variable-temperature studies of laser-initiated $^5T_2 \rightarrow {}^1A_1$ intersystem crossing in spin-crossover complexes: Empirical correlations between activation parameters and ligand structure in a series of polypyridyl ferrous complexes. *Inorg. Chem.* **1996**, *35*, 2100−2112.
27. Guionneau, P.; Marchivie, M.; Bravic, G.; Létard, J.-F.; Chasseau, D. Structural aspects of spin crossover. Example of the $[Fe^{II}L_n(NCS)_2]$ complexes. *Top. Curr. Chem.* **2004**, *234*, 97−128.
28. Holland, J.M.; McAllister, J.A.; Kilner, C.A.; Thornton-Pett, M.; Bridgeman, A.J.; Halcrow, M.A. Stereochemical effects on the spin-state transition shown by salts of $[FeL_2]^{2+}$ [*L* = 2,6-di(pyrazol-1-yl)pyridine]. *J. Chem. Soc. Dalton Trans.* **2002**, 548–554

29. Clemente-León, M.; Coronado, E.; Giménez-López, M.C.; Romero, F.M. Structural, thermal, and magnetic study of solvation processes in spin-crossover $[Fe(bpp)_2][Cr(L)(ox)_2]_2 \cdot n H_2O$ complexes. *Inorg. Chem.* **2007**, *46*, 11266–11276.
30. Amoore, J.J.M.; Kepert, C.J.; Cashion, J.D.; Moubaraki, B.; Neville, S.M.; Murray, K.S. Structural and magnetic resolution of a two-step full spin-crossover transition in a dinuclear iron(II) pyridyl-bridged compound. *Chem. Eur. J.* **2006**, *12*, 8220–8227.
31. Pritchard, R.; Kilner, C.A.; Halcrow, M.A. Iron(II) complexes with a terpyridine embrace packing motif show remarkably consistent cooperative spin-transitions. *Chem. Commun.* **2007**, 577–579.
32. Mohammed, R.; Chastanet, G.; Tuna, F.; Malkin, T.L.; Barrett, S.A.; Kilner, C.A.; Létard, J.-F.; Halcrow, M.A. The synthesis of new 2,6-di(pyrazol-1-yl)pyrazine derivatives, and the spin state behavior of their iron(II) complexes. *Eur. J. Inorg. Chem.* **2013**, 819–831.
33. Brooker, S. Spin crossover with thermal hysteresis: Practicalities and lessons learnt. *Chem. Soc. Rev.* **2015**, *44*, 2880–2892.
34. O'Connor, C.J. Magnetochemistry—Theory and experimentation. *Prog. Inorg. Chem.* **1982**, *29*, 203–283.
35. Sheldrick, G.M. A short history of *SHELX*. *Acta Crystallogr. Sect. A* **2008**, *64*, 112–122.
36. Barbour, L.J. X-Seed—A software tool for supramolecular crystallography. *J. Supramol. Chem.* **2001**, *1*, 189–191.
37. Spek, A.L. Single-crystal structure validation with the program *PLATON*. *J. Appl. Cryst.* **2003**, *36*, 7–13.